Experiments in Fluids (2024) 65:160
https://doi.org/10.1007/s00348-024-03897-8

RESEARCH ARTICLE

Enhanced three-dimensional particle detection in microcirculation experiments with defocus particle tracking and ghost red blood cells

Gonçalo Coutinho[1] · Philipp Warlitz[2] · Ana R. Silva-Santos[3] · Duarte M. Prazeres[3] · Ana Moita[1] · Jochen Kriegseis[2] · António Moreira[1] · Massimiliano Rossi[4]

Received: 19 July 2024 / Revised: 11 September 2024 / Accepted: 3 October 2024

Abstract

Experimental investigations on the motion of rigid particles in microcirculation environments are still scarce owing to the three-dimensional (3D) motion of the particles and to the particle image masking due to the presence of the red blood cells (RBCs). Despite the recent progress on the 3D tracking of rigid particles in RBC flows with defocus particle tracking (DPT) methods, the problem of particle image masking remains to be solved. Here, we propose, test, and evaluate the use hemoglobin-free RBCs, also known as ghost RBCs, as a replacement for normal RBCs in experiments with rigid particles in microcirculation environments. We performed DPT measurements of a pressure-driven flow of normal and ghost RBC suspensions seeded with rigid particles at three different flow rates. We show that the quasi-transparent appearance of ghost RBCs, as a result of the lack of hemoglobin, eliminates the RBC-induced masking of the defocused particle images and allows to achieve the particle matching standards found in cell-free experiments. In fact, ghost RBC suspensions enable the tracking of the rigid particles across the entire height of the microchannel, which was not possible in normal RBC flows. On a fluid dynamic level, we show that ghost RBC suspensions provide similar conditions to normal RBCs in terms of the velocity of the rigid particles and the rigid particles exhibit similar lateral dynamics in both types of cell suspensions. In essence, the findings from this work demonstrate that ghost RBCs are a well-suited replacement for normal RBCs in experiments aiming at deciphering the motion of rigid particles in microcirculation environments.

Graphical abstract

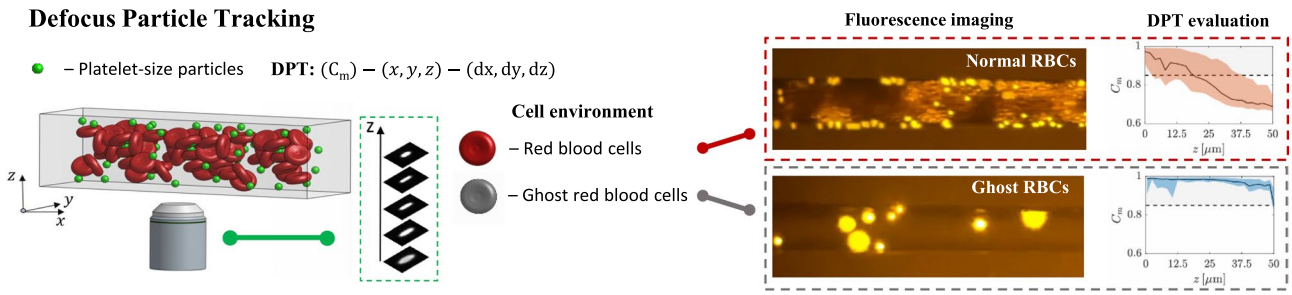

1 Introduction

The mechanisms that drive rigid particles in microcirculation have been studied since the early 1980s, beginning with the work of Schmid-Schönbein et al. (1980). These mechanisms have gained increasing attention due to their intrinsic connection to platelet lateral migration, also known as margination phenomenon, in microvascular flows (Decuzzi et al. 2005; Smyth et al. 2009; Flamm and Diamond 2012). Such mechanisms are particularly relevant to pathological conditions involving unhealthy RBCs (Glenister et al. 2002; Chang et al. 2017) and hold promise for drug delivery applications (Müller et al. 2014).

Extended author information available on the last page of the article

Published online: 28 October 2024

Over the last decade, these mechanisms have been addressed by several numerical investigations, including a lattice Boltzmann method (Crowl and Fogelson 2011), direct numerical simulations (Mehrabadi et al. 2014) or even a three-dimensional (3D) computational model (Vahidkhah et al. 2014). Yet, the number of experimental investigations is still scarce: A consequence of the challenging measurement conditions found in microcirculation experiments. On the one hand, the presence of RBCs at physiologically relevant concentrations masks the particle images of the rigid particles, making particle detection a difficult task (Carboni et al. 2016; Coutinho et al. 2023). On the other hand, rigid particles are known to move in all three dimensions in microvascular flows (Vahidkhah et al. 2014; Coutinho et al. 2023), thus narrowing the use of particle-based velocimetry to 3D methods.

When it comes to experiments, particle-based velocimetry methods are non-intrusive, optical measurement techniques, well known for providing quantitative measurements of the two-dimensional (2D) velocity. These include classical approaches such as microparticle image velocimetry (μPIV) (Lindken et al. 2009) and microparticle tracking velocimetry (μPTV) (Ohmi and Li 2000). In the context of microcirculation, these methods thus result in an oversimplification of the aforementioned 3D problem that is the motion of rigid particles in microvascular flows. To tackle the 2D limitation, Coutinho et al. (2023b) have recently shown the successful implementation of a defocus particle tracking (DPT) method known as general defocusing particle tracking (GDPT) to track rigid particles in a RBC flow in all three dimensions (Barnkob and Rossi 2020; Rossi and Barnkob 2020). Despite the progress on the 3D tracking, particle detection remained challenging owing to the presence of the RBCs, which degraded the correlation coefficient in GDPT evaluations. In addition, such masking effects were likely to be a source of position uncertainty, especially for the out-of-plane coordinate. A similar report was provided by the μPTV measurements of (Carboni et al. 2016).

A possible solution for the RBC-induced masking is the use of ghost RBCs, i.e., hemoglobin-free RBCs. Briefly, the RBCs undergo a process where the hemoglobin is removed from the cells, resulting in quasi-transparent cells with similar shape and size to normal RBCs. Due to the increased transparency, they are an attractive solution to improve particle detection in DPT measurements in microcirculation environments. It is worth noting that the use of ghost RBCs is by no means new, as they have been used in the context of microcirculation experiments (Goldsmith et al. 1995), and medical applications such as drug delivery (Zhang et al. 2022). Hence, the production process is well established in the literature see, e.g., Jamiolkowski et al. (2015).

Despite the promising use of ghost RBCs for microcirculation experiments, such a transformation might affect the fluid dynamic conditions and the dynamics of the rigid particles. In this work, we propose, test and evaluate the use of ghost RBCs as a replacement for normal RBCs in experiments with rigid particles in microcirculation environments. We performed DPT measurements of pressure-driven flows of normal and ghost RBC suspensions, seeded with rigid particles (i.e., rigid-fluorescent PS microspheres with nominal diameter of 2.47 μm). The use of the DPT method known as GDPT allowed us to obtain the 3D coordinates and velocity components of the rigid particles inside normal and ghost RBC flows. As primary goal, we aim to understand whether the use of ghost RBCs can improve the correlation coefficient in the GDPT evaluations (Sect. 3.1), while additionally comparing the fluid dynamic conditions created by both types of cell suspensions, i.e., normal and ghost RBCs, in terms of velocity data of the rigid particles (Sect. 3.2). Ultimately, we analyze the particle dynamics in normal and ghost RBCs flows according to the particle diffusivity and drift velocity (Sect. 3.3).

2 Materials and methods

2.1 Preparation of normal and ghost red blood cells samples

The RBCs suspensions were prepared from washed bovine RBCs (IBORBC100P, Innovative Research Co., USA). To obtain a hematocrit level of Hct=30 %, the initial RBC solution was diluted in phosphate-buffered saline (PBS) (×1.0, ph=7.4, FisherScientific Co., USA) (Carboni et al. 2016; Coutinho et al. 2023). Preparation of ghost RBCs was performed based on the procedure reported by (Jamiolkowski et al. 2015). Briefly, 4 mL of the RBC suspension at 30 % Hct was mixed with 36 mL of a lysing solution containing 4 mM $MgSO_4$, 25 mL/L of PBS and acetic acid until reaching a final pH of 5.2. Then, the solution was left to rest overnight at 4 °C after which the pH was brought back to the physiological norms of 7.8, followed by incubation at 37 °C for 1 h to promote cell reseal. The solution was then centrifuged at 15,000 g for 30 min and the supernatant was discarded. Ghost RBCs were washed twice with PBS buffer through centrifugation under the same aforementioned conditions. On the last washing step, the volume of ghost RBCs was determined and the volume of PBS was adjusted to a final hematocrit of 30 % in PBS with 100 mg/L gentamicin (NZYTech, Portugal). A visual comparison between the normal and ghost RBCs is already given in Fig. 1c, where we show bright-field, color-coded images of the two types of RBCs flowing inside a microchannel. Ultimately, rigid fluorescent spherical particles (530/607 nm, PS-FluoRed, MicroParticles GmbH, Germany) with a nominal diameter

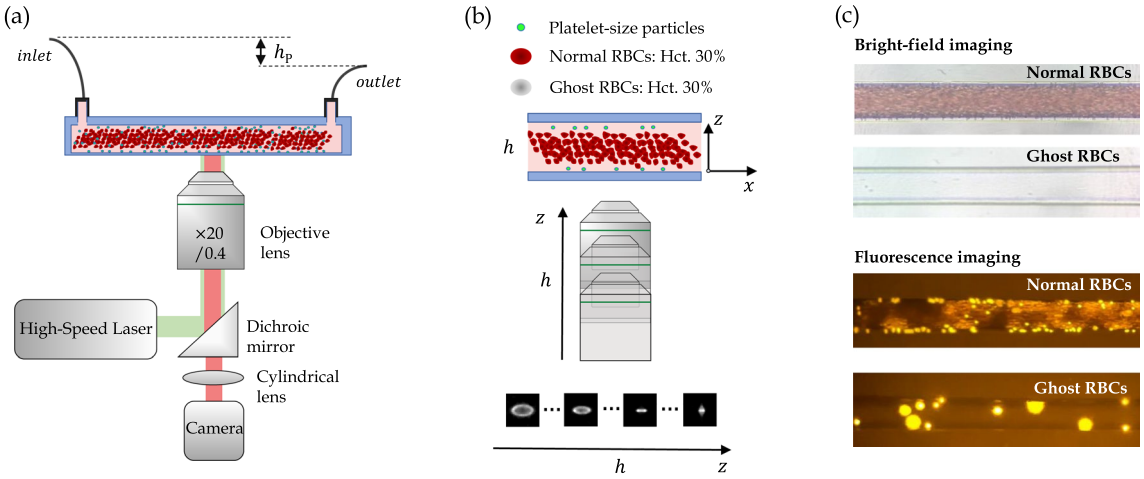

Fig. 1 (**a**) Schematic of the experimental setup used to perform the DPT measurements. (**b**) Schematic of the acquisition of the calibration image stack. (**c**) Sample color-code images of flow with normal and ghost RBCs using bright-field and fluorescence imaging without the cylindrical lens

of 2.47 µm were added to the solutions of normal and ghost RBCs samples. Henceforth, unaltered RBCs will be referred to as normal RBCs to provide a clear distinction from the ghost RBCs.

2.2 Experimental setup

The general schematic of the experimental setup is provided in Fig. 1a. The microchannel was placed on the working stage of an epi-fluorescent inverted microscope (DM IL LED, Leica Microsystems GmbH, Germany) equipped with a high-speed camera (HighSpeedStar 4 G, LaVision GmbH, Germany). The system was operated with a ×20/0.4 objective lens (NPlan Epi, Leica Microsystems GmbH, Germany), together with a cylindrical lens ($f_{cyl} = 500$ mm) (LJ1144RM-A, Thorlabs Inc., USA) placed at a distance of 60 mm in front of the camera sensor. This yielded a spatial resolution of 0.76 µm and 0.67 µm in the x- and y-direction, respectively. The present configuration used a backlight illumination provided by a high-speed laser (527 nm Nd: YLF LDY 300, Litron Lasers, UK) operated at 45%, and in synchronization with the high-speed camera through LaVision software DaVis 8. The system also included a filter cube for fluorescence imaging (Excitation: BP 525/50 nm; dichroic: 570 nm and emission: 620/60 nm). The measurements were taken in a microchannel with a square cross-sectional area of $w_{ch} \times h_{ch} = 50 \times 50\,\mu m^2$ and length of $l_{ch} = 58.5$ mm (CS-10000087, Darwin Microfluidics, France), see Fig. 1a. In all measurements, the pressure-driven flows were imposed by a constant pressure drop, which was obtained by setting three different height offsets (h_p) between the inlet and collection reservoir: $h_p = 90, 210, 460$mm. We used two large 60-mL luer-lock syringes to minimize flow variability over time. To ensure comparability between cases, we applied the same protocol to all measurements, which included setting the flow, allowing a standby period for stabilization, and ultimately performing the measurement. The resulting flow rates were characterized by measuring the Poiseuille flow of a PBS solution, i.e., with a cell-free solution: $Q = [0.14, 0.48, 0.64]$ µL/min, yielding wall-shear rates of $\dot{\gamma} = [134.49, 453.47, 609.21]$ s^{-1}, see (Son 2007). Please note that henceforth we will refer to the imposed pressure drops in terms of the corresponding reference flow rates Q_1, Q_2 and Q_3 of the PBS solution, respectively. To ensure the reproducibility of the results, the measurements were repeated three times per flow rate for the two types of cell suspensions. Between measurements, the whole system was flushed and the microchannel was rinsed with distilled water. Additionally, the cell suspensions were gently agitated before each measurement to avoid sedimentation.

2.3 Defocus particle tracking

To determine the 3D coordinates (x, y, z) and velocity components (v_x, v_y, v_z) of the rigid particles in the normal and ghost RBCs flows, we used a single-camera 3D PTV method known as GDPT (Barnkob and Rossi 2020; Rossi and Barnkob 2020). Here, x and y represent the in-plane coordinates, with x defined along the main flow direction as depicted in Fig. 1b; z is the out-of-plane component, defined along the depth of the microchannel, see Fig. 1b. For optical setups providing particle images that vary solely with out-of-plane coordinate (z), the method takes advantage from the depth-dependent shape of the defocused particle images to determine the depth position. It is worth noting that use of spherical rigid particles allows to obtain unique

defocused particle images depending solely on their position along the optical axis, i.e., their out-of-plane position, see Fig. 1b. As such, the 3D positions of the particles are recovered using a suitable mapping of the defocused particle images for the out-of-plane coordinate (z), and the in-plane coordinates (x, y) are obtained from the center of each identified the defocused particle images. The mapping consists of a calibration image stack, which in our case was obtained by taking images of a rigid particle sedimented on the bottom of the microchannel and adjusting the depth position by moving the objective lens of the microscope at constant steps of 1 micron (Fig. 1b).

The measurements were taken near the center of the microchannel ($\Delta x = 29$ mm; $\Delta x/l_{\mathrm{ch}} \approx 50\,\%$) and the flow was recorded using a total of 6000 images of the rigid particles, with the frame rate adjusted between 350 Hz and 650 Hz depending on the working fluid and flow rate. The size of the field-of-view (FOV) was 1024×256 pixels, yielding a total length of 778 mm across the main-flow direction. The images were then processed using the DefocusTracker software (Barnkob and Rossi 2021), an implementation of the aforementioned DPT method known as GDPT. As such, the particle detection is performed by matching the experimental to the calibration images, through normalized cross-correlation (Lewis 1994). For each defocused particle image, the correlation coefficient (C_m) translates the goodness of the particle image matching and takes values between 0 and 1, with 1 corresponding to a perfect match (Rossi and Barnkob 2020). We will continue the discussion later in Sect. 3.1. Again, the in-plane coordinates (x, y) correspond to the center of the defocused particle image. As for the tracking, we used the nearest-neighbor algorithm (Malik et al. 1993), since the particle density was low. The reader can have access to DefocusTracker software through the treatise of (Barnkob and Rossi 2021). Ultimately, the measurement uncertainty was estimated using a reference measurement of a Poiseuille flow (i.e., PBS measurement), as in Barnkob and Rossi (2020). In particular, considering the displacements in y- and z-direction, taking a null-displacement as the true value. We obtained the following uncertainties $\sigma_{x,y} = 0.15\,\mu$m and $\sigma_z = 0.4\,\mu$m.

2.4 Correction of bias errors

In DPT experiments in microfluidic environments, the measured out-of-plane coordinate (z) is typically biased due to the presence of the field curvature aberration and refraction (Cierpka et al. 2010; Rossi et al. 2012). Regarding the former, the particle coordinate was corrected using a procedure based on a reference measurement of a Poiseuille flow, i.e., using the PBS measurements, as described in Coutinho et al. (2023a). Briefly, this approach allows to model the field curvature across the FOV using particle trajectories and velocity, and then retrieve the correction for this bias error. As for refraction, it was corrected using the refractive index of PBS, which is approximately: $n_{\mathrm{PBS}} = 1.33$. It is worth noting that the impact of the refractive index of the two types of cells is not meaningful. In fact, this can be verified later in Fig. 4, where after correcting for refraction using the refractive index of PBS, the distribution of the data points across the out-of-plane coordinate (z) yields already approximately the height of the microchannel. If the refraction of light through these types of cells was meaningful, we would expect a mismatch between the height of the data and the microchannel. For more details on the bias errors, the reader should refer to Coutinho et al. (2023a).

2.5 Statistical significance

To show that our DPT measurements achieved a statistically meaningful basis for the evaluation of the particle dynamics, specifically for the particle lateral drift (v_y) and particle diffusivity (D_y) shown later in Sect. 3.3, we evaluated the standard deviation of the lateral velocity (σ_{v_y}) of the rigid particles, normalized with the characteristic velocity of the flow v_x as a function of systematically increased sample number (N). It is worth noting that this quantity translates the variability of the particle lateral drift (v_y), and since our flow is laminar, it is a combination of velocity fluctuations plus uncertainty.

The evaluation was performed using the particle tracking data from the bottom half of the microchannel ($z < 25\,\mu$m) and in two characteristic regions across the width: one located at $y \approx 0\,\mu$m matching the center of the flow, another at $y \approx 12.5\,\mu$m ($75\,\% w_{\mathrm{ch}}$), where the particle diffusivity is expected to be larger (Coutinho et al. 2023b), see Fig. 4. The choice of limiting the z information derives from the expected C_m degradation with the out-of-plane coordinate (z), which thus influences the accuracy on the particle location, as shown later in Sect. 3.1. For the two characteristic regions, we considered a y-bin with a total width of 4 microns. A similar binning procedure was applied by Coutinho et al. (2023b) to evaluate the particle dynamics in RBC flows. The results are shown in Fig. 2a and b as a function of the number of data points N per bin, for normal and ghost RBCs. Figure 2 shows that the normalized standard deviation (σ_{v_y}) approaches a plateau for increasing N, thus ensuring that our data have a statistically meaningful basis for the evaluation of the particle dynamics. From a different perspective, normal RBCs exhibit a significantly larger standard deviation (σ_{v_y}) compared to ghost RBCs, indicating a higher level of uncertainty for normal RBCs. Such a result is likely a direct consequence of the RBC masking.

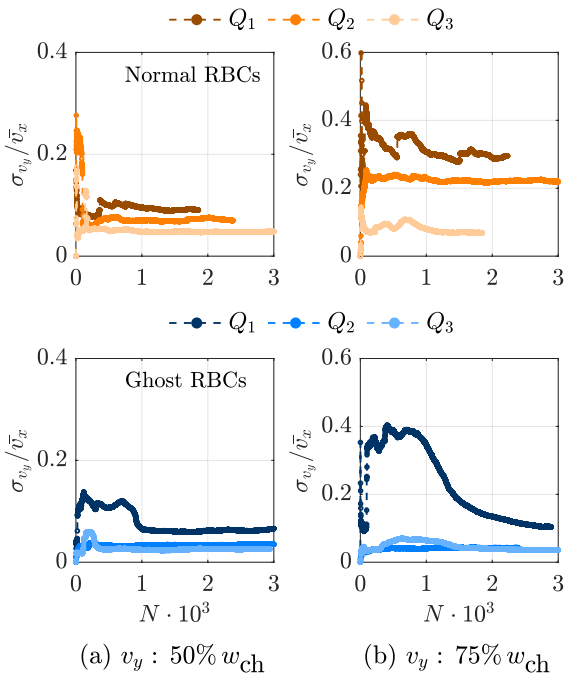

Fig. 2 Convergence of standard deviation of particle lateral velocity (σ_{v_y}) normalized with the characteristic velocity of the flow (v_x) for the recorded number of data points (N) per bin, for normal and ghost RBCs. (**a**) Bin located: $y \approx 0$ µm (50 % w_{ch}). (**b**) Bin located: $y \approx 12.5$ µm (75 % w_{ch})

3 Results and discussion

3.1 Correlation coefficient in GDPT measurements

To evaluate the impact of the presence of normal and ghost RBCs in the detection of rigid particles, Fig. 3 shows the correlation coefficient (C_m) as a function of the out-of-plane coordinate (z), obtained from the GDPT evaluations for the considered flow rates (Q_{1-3}). The results are shown for a single measurement and include the median value of C_m and 80 % distribution of the dataset. Please note that as introduced in Sect. 2.3, C_m varies between 0 and 1, where 1 corresponds to a perfect match of the defocused particle image.

As recently observed by Coutinho et al. (2023b), in the presence of normal RBCs the data show a large dispersion and we can observe a degradation of C_m as z increases (first row in Fig. 3). This comes as a consequence of the increasing number of RBCs flowing between the particle and the objective lens, as the particle located at a higher z coordinate, i.e., deeper into the flow. In practical terms, this influences the particle matching, the determination of the out-of-plane coordinate (z), and therefore the position accuracy. To minimize such effects and following our previous work (Coutinho et al. 2023b), we imposed a threshold at $C_m = 0.85$ to exclude the coarser particle matches, as depicted by the black-dashed line in Fig. 3. Despite excluding those coarser particle matches, normal RBCs still exhibit larger scatter and lower correlation coefficients for a given out-of-plane coordinate (z), i.e., compared to ghost RBCs. In other words, ghost RBCs have a better z-position accuracy.

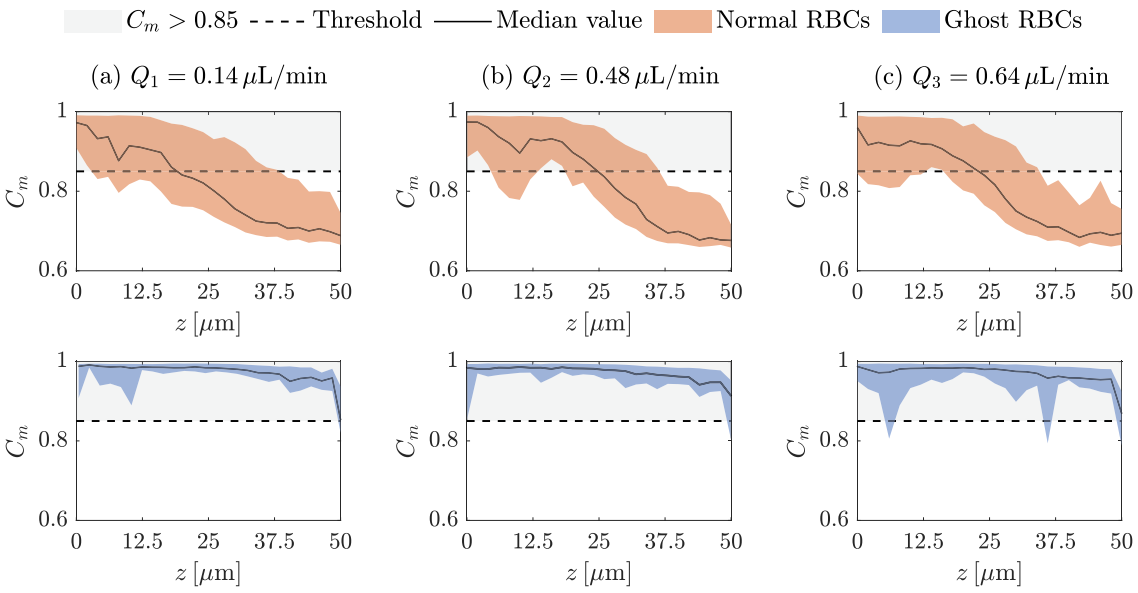

Fig. 3 Distribution of the correlation coefficient (C_m) as a function of z obtained from the GDPT evaluations for normal and ghost RBCs at different flow rates. (**a**) $Q_1 = 0.14$ µL/min. (**b**) $Q_2 = 0.48$ µL/min. (**c**) $Q_3 = 0.64$ µL/min

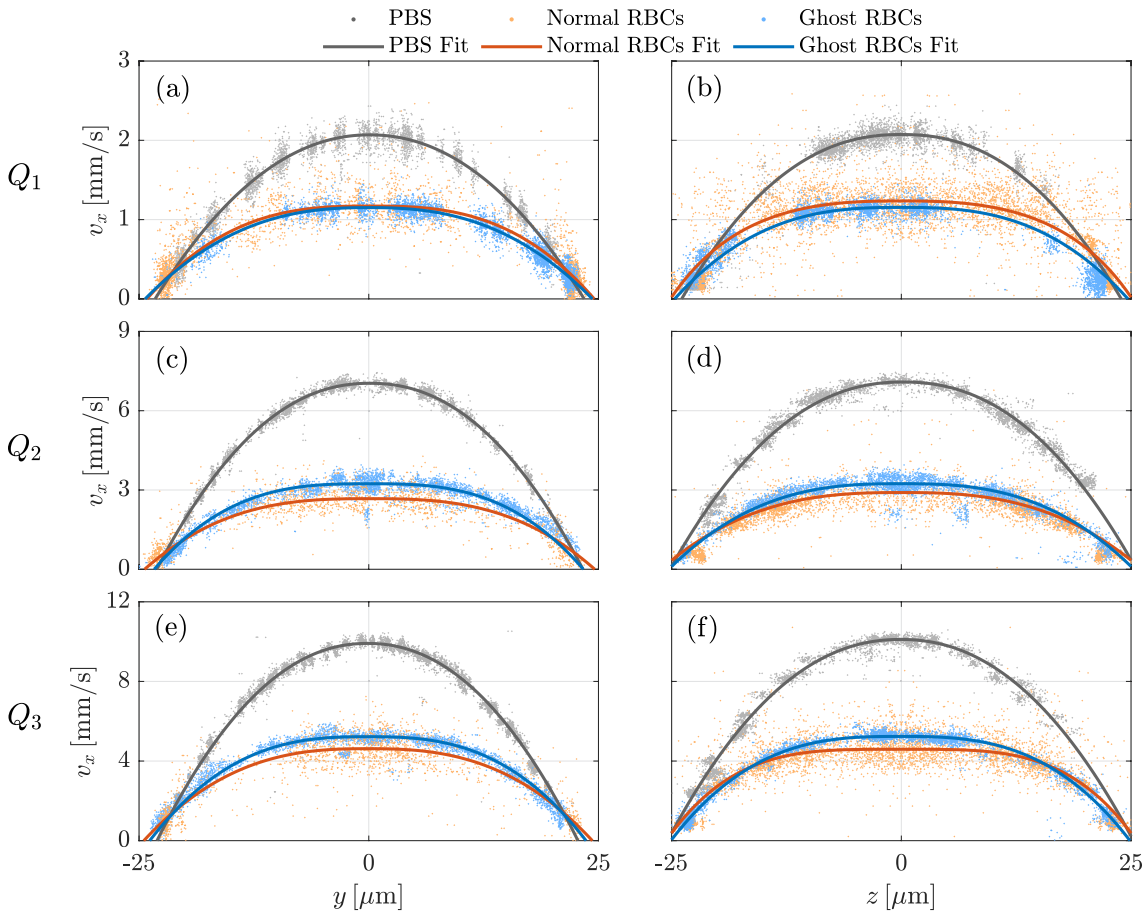

Fig. 4 Scatter and fitted velocity profiles ($v_x(y)$, $v_x(z)$) of the rigid particles based on Eq. (1), including the measurements in PBS, normal and ghost RBC suspensions for the three flow rates: Q_1, Q_2, and Q_3. (**a**), (**c**) and (**e**) $v_x(y)$ for $z \in [-1.5, 1.5]$ µm. (**b**), (**d**) and (**f**) $v_x(z)$ for $y \in [-1.5, 1.5]$ µm

Additionally, they exhibit correlation coefficients in the range of those found in cell-free experiments (not shown). Briefly, cell-free experiments have a small scatter of the correlation coefficient (C_m), with values ranging above a threshold of 0.9 and which are rather constant for the given out-of-plane coordinate (z) see, e.g., Barnkob and Rossi (2020), and Coutinho et al. (2023b). These standards are what allow to retrieve the out-of-plane coordinate across the entire height of the microchannel, hence allow ghost RBCs to surpass the measurement limitations found in experiments with rigid particles and normal RBCs. In Sect. 3.2, we compare the fluid dynamic conditions created by the two types of cell suspensions based on the velocity data of the rigid particles.

3.2 Flow characterization

On a fluid dynamic level, we want to understand whether ghost RBCs provide a similar conditions to that of normal RBC suspensions. To that end, we compared the velocity profiles $v_x(y)$ and $v_x(z)$ of the rigid particles in normal and ghost RBCs suspensions for the different flow rates. Accordingly, we defined a slice with 3 microns in height around the center of the microchannel (i.e., $-1.5 < z < 1.5$ µm), projected the velocity data along the y direction and fitted to an empirical equation derived from the solution of the Poiseuille flow in straight-square microchannels

$$v_x = v\left(\frac{\cosh(0.5^m) - \cosh(|y^*|^m)}{\cosh(0.5^m) - 1}\right) + v_0, \tag{1}$$

where v and v_0 are the fitting parameters based on the velocity distribution (v_x), and m, is a fitting parameter based on the velocity profile bluntness (see, e.g., Passos et al. 2019). The coordinate y^* was normalized with the width of the microchannel (w_{ch}). A similar procedure was applied for z, yet with the slice defined along the width ($-1.5 < y < 1.5$ µm) and using the height of the microchannel (h_{ch}) for normalization. For normal RBC suspensions, we have additionally assumed symmetry in the z-direction, and the measured data were mirrored on the center of the microchannel to

compensate for missing particle tracking information in the depth of the microchannel. Again, this is a consequence of the RBC masking, which forces to exclude particle tracking data below a given z, based on the degradation of the correlation coefficient (Sect. 3.1). The results are shown in Fig. 4. For comparison, we also plot the velocity data from the measurement on the PBS solution, i.e., the cell-free suspension. Please note that the discrete locations of velocity data in Fig. 4 are an intrinsic consequence of the single frame particle tracking measurements, which provide a sparse distribution of particle coordinates across the measurement volume, with this effect becoming even more pronounced as we only plot a slice of our data points.

The difference between PBS and the two types of cell suspensions is remarkable. While for the PBS measurements, the velocity information resembles a Poiseuille flow (Bruus 2008),, for the normal and ghost RBCs—in contrast—we can observe a significantly blunter velocity profile, as typical for RBCs flows in microchannels. Such blunter profile is consistent with previous in-vitro studies (Lima et al. 2008; Roman et al. 2012; Carboni et al. 2016) and arises most likely due to the larger number of RBCs flowing around the centerline of the microchannel. Comparing the cell suspensions, the results shown in Fig. 4 highlight the resemblance between the fluid dynamic conditions created by ghost and normal RBCs, specially in terms of the shape of the velocity profiles. Furthermore, the measurements in ghost RBC suspensions result in a smaller scatter of the velocity data and allow to retrieve the velocity data across the entire depth of the microchannel.

As for the magnitude, we do observe a minor increase of the particle velocity in ghost RBC suspensions. This evaluation can be also done on Fig. 5a, where we compare the maximum velocity, calculated using the fitted curves from Fig. 4. The results represent the mean value of the consecutive measurements, and the error bars show the root mean square of error (rmse) from the fitting function. This difference in the magnitude can be attributed to two different causes. First and more importantly, owing to a difference in the mechanical properties of the cells. As a consequence of the manufacturing process of ghost RBCs, which includes the removal of hemoglobin, the membrane mechanical properties and the dynamic behavior of the cells might be affected (Lima et al. 2008). In fact, Nash and Meiselman (1983) showed experimentally that ghost RBCs have different elastic modulus than normal RBCs. Another possible, yet minor, contributor could be a slight difference between the concentration of the two cell suspensions (i.e., Hct), which would influence the fluid viscosity, hence the velocity magnitude. The influence of Hct on the velocity profiles is a well-known phenomenon as shown by, for instance, the experiments of (Passos et al. 2019). Additionally, the larger error bars for the normal RBCs are most likely a consequence of the larger

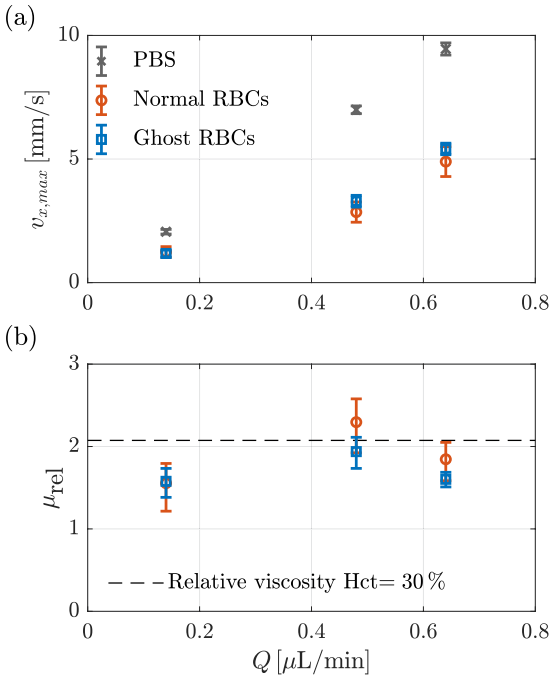

Fig. 5 (**a**) Maximum velocity ($v_{x,max}$) for the PBS, normal and ghost RBCs measurements, including the three flow rates. (**b**) Relative viscosity of normal and ghost RBCs, for the three flow rates. The reference line represents the expected relative viscosity based on the empirical model from Pries et al. 1992, for RBC flows in a capillary-sized microchannel (D_{ch} = 55 µm) at Hct=30%. Error bars are included based on the root mean square of the error from the velocity fitting function

uncertainty as discussed in Sect. 2.5, as well as lower position accuracy as elaborated in Sect. 3.1, both owing to the RBC-induced masking.

Another relevant property of these cell suspensions is viscosity. It is well known that the viscosity of RBC suspensions increases with Hct (Pries et al. 1992; Fitzgibbon et al. 2015), thus being also a term of comparison between normal and ghost RBCs. Since RBC flows have a non-Newtonian behavior in microchannels, the viscosity is here calculated as a relative viscosity (μ_{rel}) (Bagchi 2007; Coutinho et al. 2023b). Following the work of Pries et al. (1992), the expression for the relative viscosity yields the ratio between flow rates of PBS and RBCs according to

$$\mu_{rel} = \frac{Q_{PBS}}{Q_{RBC}}, \tag{2}$$

where Q_{RBC} and Q_{PBS} represent the flow rate with and without flowing RBCs, respectively. Equation (3) was computed by the ratio between the line integral of the velocity profiles $v_x(y)$ along the y-direction for the PBS and RBC measurements. Please note that this ratio allows to estimate the relation between the given flow rates, while effectively handling

the complexities associated with non-Newtonian fluids. More details are also given in Coutinho et al. (2023b). The same expression is valid for the ghost RBCs. For comparison with previous studies, we compare the measured values of the relative viscosity with the empirical model given by Pries et al. (1992), i.e.,

$$\mu_{\text{rel}} = 1 + B[(1 - \text{Hct})^C - 1]. \tag{3}$$

The fitting parameters B and C were obtained from the measurements of Bayliss (1952) in a microchannel with a tube diameter of $D_{\text{ch}} = 55\,\mu\text{m}$. These values were selected based on the available data since the conditions were similar to the current experiments ($B = 3.54$; $C = -0.743$). The results of the relative viscosity (μ_{rel}) including all three flow rates are shown in Fig. 5b and represent a mean value. The added error bars are based on the rmse from the velocity fitting function (Eq. 1). The results from Fig. 5b likewise show some minor differences between normal and ghost RBCs, yet within the rmse of the velocity fitting function. In addition, the measured values show a good correlation with the empirical model, as shown by the dashed-black line.

Despite these small differences between the two types of cells, the present results show the break-off point for choosing ghosts over normal RBCs, and why the former are a preferable choice for experiments aiming at deciphering the motion of rigid particles in microcirculation environments: improved particle matching and similar fluid dynamic conditions. More importantly, the motion of rigid particles in microcirculation environments is 3D and not being able to retrieve the particle tracking data across the entire height of the microchannel in normal RBC suspensions can be a drawback, as noted by Coutinho et al. (2023b).

3.3 Particle diffusivity and drift velocity

Another relevant phenomenon when aiming to decipher the motion of rigid particles in microcirculation environments is the lateral motion, which is closely linked to the so-called margination phenomenon (Decuzzi et al. 2005; Flamm and Diamond 2012) and it is typically described by particle diffusivity, as well as the particle drift velocity. Following previous works (Crowl and Fogelson 2011; Závodszky et al. 2019; Coutinho et al. 2023b), the particle diffusivity (D_y) is hereby estimated assuming that the particle movement in these types of cell suspensions follows a standard diffusion process, and it can be computed from the mean square displacement as a function of time according to the following equation

$$D_y = \frac{1}{N}\sum_{i=1}^{N}\frac{[y_i(t_0 + \Delta t) - y_i(t_0)]^2}{2\Delta t}, \tag{4}$$

where N is the number of tracked particles, y_i the particle coordinate at a given time, t_0 the reference time, and Δt represents the interval between consecutive frames. Since our measurements were taken at different camera frequencies (Sect. 2.2), we selected a time interval of 6 ms, to ensure comparability between all datasets. Please note that in this type of measurements, the particle tracking data are retrieved at discrete time samples. Besides, it is assumed that a 6-ms time interval captures several collision events between the cells and the particles, see, e.g., Závodszky et al. (2019). The values of D_y are averaged in space along the main flow direction x. For the calculation itself (D_y), the microchannel width ($w_{ch} = 50\,\mu$ m) was divided into bins of equal size, with a total width of 3 µm and considering a bin overlap of 50 %. Since the results for the z coordinate are conditioned by the RBC-induced masking (Sect. 3.1), and to ensure comparability between the normal and ghost RBCs flow results, we only considered the data points within the bottom half of the microchannel. In other words, a boundary threshold was imposed at the middle plane of the microchannel (i.e., $z < 25$ µm). A similar procedure was used by Coutinho et al. (2023b) due to the same masking effects of the RBCs. Moreover, for the present analysis, we focus solely on the y coordinate. As discussed in Sect. 3.1 and by Coutinho et al. 2023b, based on the correlation coefficient we can anticipate a poorer position accuracy for the out-of-plane coordinate (z), which in turn makes comparisons between normal and ghost RBCs suspensions challenging. It is worth noting that the particle diffusivity was also estimated from the measurements with a PBS solution (i.e., absence of cells) and it is in the order of $\mathcal{O}^{-8}$ cm^2/s (not shown). These values range an order of magnitude lower than the RBC-induced diffusivity shown in Fig. 6, where, e.g., for Q_3 it yields 3.5×10^{-7} cm^2/s.

Figure 6 shows a comparison between the distribution of the particle diffusivity (D_y) in the normal and ghost RBC suspensions for all three flow rates. As demonstrated by the previous numerical simulations (Crowl and Fogelson 2011; Mehrabadi et al. 2014; Závodszky et al. 2019) and more recently with an experimental campaign by our group (Coutinho et al. 2023b), the distribution of the particle diffusivity in normal RBCs flows is non-uniform and underlines a region of higher diffusivity around the center of the microchannel. Approaching the wall of the microchannel, it depicts a steep gradient: A consequence of the decreasing number of RBCs as one approaches the wall (Grandchamp et al. 2013; Mehrabadi et al. 2014). Regarding the magnitude of the particle diffusivity, for the lower flow rate Q_1 ($\dot{\gamma} = 134.49$ s^{-1}), this is in the order of magnitude of that reported in our previous experiments, which were performed in the same flow conditions (Coutinho et al. 2023b). Similar conclusions are drawn for $\dot{\gamma} = 400$ s^{-1} and the values reported by the numerical simulations of Crowl and Fogelson (2011) in a two-dimensional microchannel with a total

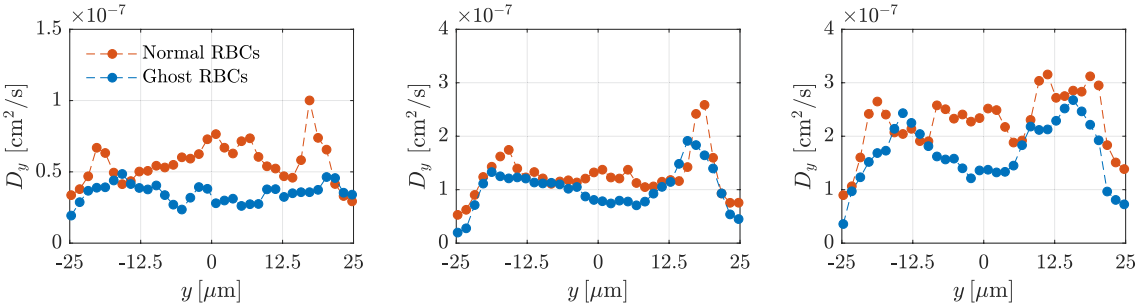

Fig. 6 Comparison of the particle diffusivity (D_y) across the width of the microchannel (y) in normal and ghost RBC flows, considering a time interval of $\Delta t \approx 0.006$s. (**a**) $Q_1 = 0.14\,\mu$L/min. (**b**) $Q_2 = 0.48\,\mu$L/min. (**c**) $Q_3 = 0.64\,\mu$L/min

width of 50 microns. In addition, we can also observe the increase in the particle diffusivity with flow rate as similarly reported by Crowl and Fogelson (2011).

By comparing the distribution of particle diffusivity in normal and ghost RBC suspensions, we can identify the resemblance between cases. Similar to normal RBCs, the results in ghost RBCs flow also exhibit a region of higher diffusivity around the center of the microchannel, and a steep descent close to the wall. It is worth noting that due to the random and unpredictable nature of the cells and particle interactions (Vahidkhah et al. 2014; Závodszky et al. 2019), it is difficult to expect the exact same shape for the particle diffusivity, despite the proven statistical signification (see Sect. 2.5). In terms of magnitude, we observe a minor decrease in the particle diffusivity in ghost RBC suspensions. As discussed in Sect. 3.2, this decrease can be attributed to two different factors: A difference in the ghost RBCs viscosity due to the manufacturing process and to a difference between the concentration of the two cell suspensions. On a different perspective, the RBC-induced masking could also contribute to the uncertainty as discussed in Sect. 2.5, thus increasing the measured particle diffusivity. Nonetheless, the particle diffusivity in ghost RBC suspensions is within the same range as for normal RBCs. Hence, the position of ghost RBCs is strengthened as well-suited replacement for the normal RBCs in experiments with rigid particles in microcirculation environments.

As for the drift velocity (v_y), it might be worth noting that the particle diffusivity is given by $D_y = v_y^2/2$, which essentially erases the sign of v_y in D_y (see, e.g., Závodszky et al. 2019). Here, the drift velocity was estimated using the same bins and time interval Δt as in the particle diffusivity; see Eq. (4). The results are only shown in Fig. 7 for the largest flow rate (Q_3) since all results pointed to the same conclusion, i.e., there is no clear trend in the particle drift velocity. This has been already reported by Coutinho et al. (2023b). Briefly, in fully developed flow conditions and with fewer number of particles moving laterally to the region near the wall, i.e., with scarce occurrences of the margination phenomenon within the FOV, it is difficult to expect a trend.

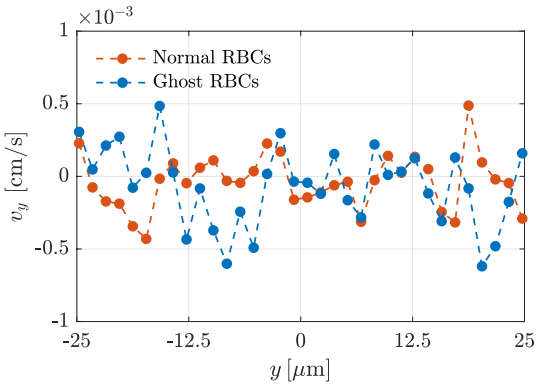

Fig. 7 Mean drift velocity (v_y) along the width of the microchannel (y) in normal and ghost RBC flows, evaluated for the highest flow rate: $Q_3 = 0.64\,\mu$L/min

4 Conclusion

In this work, we proposed, tested and evaluated the use of ghost RBCs as a replacement for normal RBCs in DPT experiments aiming at deciphering the motion of rigid particles in microcirculation environments. As recently reported by our group (Coutinho et al. 2023b), when using normal RBCs the detection of rigid particles becomes challenging due to RBC-induced masking. Here, we show that by using ghost RBCs this measurement limitation can be surpassed, with the correlation coefficient from the GDPT evaluations being improved to values similar to those found in cell-free experiments. Simultaneously, this improvement on the correlation coefficient (C_m), which implies an improvement on the particle matching, contributes to a better position accuracy of the out-of-plane

coordinate z as well. Additionally, whereas normal RBCs force to exclude the particle tracking data below a given z, ghost RBCs allow to retrieve particle tracking data across the entire height of the microchannel, thus overcoming the measurement limitations imposed by normal RBCs. This has been pointed as a major drawback for normal RBCs in this type of experiments, especially owing to the fact that the motion of rigid particles in microcirculation environments is 3D.

On a fluid dynamic level, we compared the velocity profiles of the rigid particles in normal and ghost RBC suspensions. We showed that the velocity profiles of the rigid particles in normal and ghost RBC suspensions have similar shape, yet we observed a minor decrease in the magnitude. A difference between the two types of cell suspensions was also observed in the relative viscosity. These differences were attributed to two possible causes. One is the manufacturing process of ghost RBCs which alters the mechanical properties of the cells. Second is a difference between the concentration of the two cell suspensions. The difference magnitude was likewise observed on the analysis of the particle dynamics, more specifically on the particle diffusivity. Nonetheless, we observed the resemblance between the distribution of the particle diffusivity in normal and ghost RBCs. Additionally, both shape and order of magnitude are in agreement with previous works. Altogether the break-off point for choosing ghost over normal RBCs is strengthened. However, care should be taken when interpreting these results, since ghost RBCs are not a well-suited replacement for normal RBCs in every experiment, note that our work focused solely on the motion of rigid particles in microcirculation environments.

Overall, the present work shows that ghost RBC suspensions are a well-suited replacement for normal RBCs in experiments aiming at deciphering the motion of rigid particles in microcirculation environments. Besides providing the same fluid dynamic conditions and particle dynamics, ghost RBCs allow to obtain correlation coefficients similar to those found in cell-free experiments and enable to retrieve the particle tracking data across the entire measurement height, therefore surpassing the aforementioned drawbacks associated with normal RBCs and setting new standards for these type of experiments.

Acknowledgements G.C. acknowledges the PhD scholarship 2021.04780.BD granted by Fundação para a Ciência e Tecnologia (FCT). M.R. acknowledges the financial support by the VILLUM foundation (grant no. 00036098.). G.C., A.M. and A.M. acknowledge Fundação para a Ciência e a Tecnologia (FCT) for partially financing the research trough Project Ref. PTDC/EME-TED/7801/2020 and for partially financing her contract through CEECINST/00043/2021/CP2797/CT0005, doi: 10.54499/CEECINST/00043/2021/CP2797/CT0005.

Author contribution GC contributed to conceptualization, cell preparation, data acquisition, data evaluation, writing - original draft, PW contributed to cell preparation, data acquisition, data evaluation, writing–original draft, ARSS contributed to cell preparation and writing–review, DMP contributed to cell preparation and writing–review, AM contributed to conceptualization, data evaluation, supervision and writing - review, JK contributed to conceptualization, data evaluation, supervision and writing–review and editing, ALNM contributed to supervision and writing–review, MR contributed to conceptualization, data evaluation, supervision and writing–review and editing.

Funding Open access funding provided by FCT|FCCN (b-on).

Data availability The measurement data are available upon reasonable request.

Declarations

Conflict of interest The authors declare no conflict of interest.

References

Bagchi P (2007) Mesoscale simulation of blood flow in small vessels. Biophys J 92(6):1858–1877. https://doi.org/10.1529/biophysj.106.095042

Barnkob R, Rossi M (2020) General defocusing particle tracking: fundamentals and uncertainty assessment. Exp Fluids 61(4):110. https://doi.org/10.1088/1361-6501/abad71

Barnkob R, Rossi M (2021) Defocustracker: a modular toolbox for defocusing-based, single-camera, 3d particle tracking. J Open Res Softw 9(1):22. https://doi.org/10.5334/jors.351

Bayliss L (1952) Rheology of blood and lymph. Deformation and Flow in Biological Systems pp 355–418. 10.1093/aibsbulletin/2.5.13-b

Bruus H (2008) Theoretical microfluidics. Oxford University Press. https://doi.org/10.1093/oso/9780199235087.001.0001

Carboni E, Bognet B, Bouchillon GM et al (2016) Direct tracking of particles and quantification of margination in blood flow. Biophys J 111:1487–1495. https://doi.org/10.1016/j.bpj.2016.08.026

Chang HY, Li X, Karniadakis G (2017) Modeling of biomechanics and biorheology of red blood cells in type-2 diabetes mellitus. Biophys J 113:481–490. https://doi.org/10.1101/132134

Cierpka C, Rossi M, Segura R et al (2010) On the calibration of astigmatism particle tracking velocimetry for microflows. Meas Sci Technol 22(1):015,401. https://doi.org/10.1088/0957-0233/22/1/015401

Coutinho G, Moita A, Ribeiro A et al (2023a) On the characterization of bias errors in defocusing-based 3d particle tracking

velocimetry for microfluidics. Exp Fluids. https://doi.org/10.1007/s00348-023-03635-6
Coutinho G, Moita AS, Rossi M et al (2023b) Experimental perspective on the mechanisms for near-wall accumulation of platelet-size particles in pressure-driven red blood cell suspension flows. Phys Rev Fluids 8(103):101. https://doi.org/10.1103/PhysRevFluids.8.103101
Crowl L, Fogelson AL (2011) Analysis of mechanisms for platelet near-wall excess under arterial blood flow conditions. J Fluid Mech 676:348–375. https://doi.org/10.1017/jfm.2011.54
Decuzzi P, Lee S, Bhushan B et al (2005) A theoretical model for the margination of particles within blood vessels. Ann Biomed Eng 33:179–90. https://doi.org/10.1007/s10439-005-8976-5
Fitzgibbon S, Spann A, Qi Q et al (2015) In vitro measurement of particle margination in the microchannel flow: effect of varying hematocrit. Biophys J 108(10):2601–2608. https://doi.org/10.1016/j.bpj.2015.04.013
Flamm M, Diamond S (2012) Multiscale systems biology and physics of thrombosis under flow. Ann Biomed Eng 40:2355–64. https://doi.org/10.1007/s10439-012-0557-9
Glenister F, Coppel R, Cowman A et al (2002) Contribution of parasite proteins to altered mechanical properties of malaria-infected red blood cells. Blood 99:1060–3. https://doi.org/10.1182/blood.V99.3.1060
Goldsmith H, Bell D, Braovac S et al (1995) Physical and chemical effects of red cells in the shear-induced aggregation of human platelets. Biophys J 69:1584–95. https://doi.org/10.1016/S0006-3495(95)80031-7
Grandchamp X, Coupier G, Srivastav A et al (2013) Lift and down-gradient shear-induced diffusion in red blood cell suspensions. Phys Rev Lett 110(108):101. https://doi.org/10.1103/PhysRevLett.110.108101
Jamiolkowski M, Woolley J, Kameneva M et al (2015) Real time visualization and characterization of platelet deposition under flow onto clinically-relevant opaque surfaces. J Biomed Mater Res Part A. https://doi.org/10.1002/jbm.a.35202
Lewis J (1994) Fast template matching. Vision Interface 95
Lima R, Wada S, Tanaka S et al (2008) In vitro blood flow in a rectangular pdms microchannel: Experimental observations using a confocal micro-piv system. Biomed Microdev 10:153–67. https://doi.org/10.1007/s10544-007-9121-z
Lima R, Ishikawa T, Imai Y et al (2008) Radial dispersion of red blood cells in blood flowing through glass capillaries: the role of hematocrit and geometry. J Biomech 41:2188–96. https://doi.org/10.1016/j.jbiomech.2008.04.033
Lindken R, Rossi M, Große S et al (2009) Micro-particle image velocimetry (piv): recent developments, applications, and guidelines. Lab Chip 9:2551–67. https://doi.org/10.1039/b906558j
Malik N, Dracos T, Papantoniou D (1993) Particle tracking velocimetry in three-dimensional flows - part ii: particle tracking. Exp Fluids 15:279–294. https://doi.org/10.1007/BF00223406
Mehrabadi M, Ku D, Aidun C (2014) A continuum model for platelet transport in flowing blood based on direct numerical simulations of cellular blood flow. Ann Biomed Eng 43:1410–1421. https://doi.org/10.1007/s10439-014-1168-4
Müller K, Fedosov D, Gompper G (2014) Margination of micro- and nano-particles in blood flow and its effect on drug delivery. Sci Rep 4:4871. https://doi.org/10.1038/srep04871
Nash G, Meiselman H (1983) Red cell and ghost viscoelasticity. effects of hemoglobin concentration and in vivo aging. Biophys J 43:63–73. https://doi.org/10.1016/S0006-3495(83)84324-0
Ohmi K, Li HY (2000) Particle-tracking velocimetry with new algorithm. Meas Sci Technol 11:603. https://doi.org/10.1088/0957-0233/11/6/303
Passos A, Sherwood J, Kaliviotis E et al (2019) The effect of deformability on the microscale flow behavior of red blood cell suspensions. Phys Fluids 31(091):903. https://doi.org/10.1063/1.5111189
Pries AR, Neuhaus D, Gaehtgens P (1992) Blood viscosity in tube flow: dependence on diameter and hematocrit. Am J Physiol Heart Circ Physiol 263(6):H1770–H1778. https://doi.org/10.1152/ajpheart.1992.263.6.H1770
Roman S, Lorthois S, Duru P et al (2012) Velocimetry of red blood cells in microvessels by the dual-slit method: effect of velocity gradients. Microvasc Res 84:249–261. https://doi.org/10.1016/j.mvr.2012.08.006
Rossi M, Barnkob R (2020) A fast and robust algorithm for general defocusing particle tracking. Meas Sci Technol 32(1):014,001. https://doi.org/10.1088/1361-6501/abad71
Rossi M, Segura CR, Cierpka Kähler C (2012) On the effect of particle image intensity and image preprocessing on the depth of correlation in micro-PIV. Exp Fluids 52:1063–1075. https://doi.org/10.1007/s00348-011-1194-z
Schmid-Schönbein G, Usami S, Skalak R et al (1980) The interaction of leukocytes and erythrocytes in capillary and postcapillary vessels. Microvasc Res 19:45–70. https://doi.org/10.1016/0026-2862(80)90083-7
Smyth SS, Mcever RP, Weyrich AS et al (2009) Platelet functions beyond hemostasis. J Thromb Haemost 7(11):1759–1766. https://doi.org/10.1111/j.1538-7836.2009.03586.x
Son Y (2007) Determination of shear viscosity and shear rate from pressure drop and flow rate relationship in a rectangular channel. Polymer 48:632–637. https://doi.org/10.1016/j.polymer.2006.11.048
Vahidkhah K, Diamond SL, Bagchi P (2014) Platelet dynamics in three-dimensional simulation of whole blood. Biophys J 106(11):2529–2540. https://doi.org/10.1016/j.bpj.2014.04.028
Zhang E, Phan P, Algarni H et al (2022) Red blood cell inspired strategies for drug delivery: emerging concepts and new advances. Pharm Res 39:1–26. https://doi.org/10.1007/s11095-022-03328-5
Závodszky G, van Rooij B, Czaja B et al (2019) Red blood cell and platelet diffusivity and margination in the presence of cross-stream gradients in blood flows. Phys Fluids. https://doi.org/10.1063/1.5085881

Authors and Affiliations

Gonçalo Coutinho[1] · Philipp Warlitz[2] · Ana R. Silva-Santos[3] · Duarte M. Prazeres[3] · Ana Moita[1] · Jochen Kriegseis[2] · António Moreira[1] · Massimiliano Rossi[4]

✉ Gonçalo Coutinho
goncalo.coutinho@tecnico.ulisboa.pt

Philipp Warlitz
philipp.warlitz@outlook.de

Ana R. Silva-Santos
ana.rita.santos@tecnico.ulisboa.pt

Duarte M. Prazeres
miguelprazeres@tecnico.ulisboa.pt

Ana Moita
anamoita@tecnico.ulisboa.pt

Jochen Kriegseis
jochen.kriegseis@kit.edu

António Moreira
aluismoreira@tecnico.ulisboa.pt

Massimiliano Rossi
massimiliano.rossi13@unibo.it

[1] IN+ Center for Innovation, Technology and Policy Research, Instituto Superior Técnico, University of Lisbon, Avenida Rovisco Pais, Lisbon 1049-001, Portugal

[2] Institute of Fluid Mechanics (ISTM), Karlsruhe Institute of Technology (KIT), Karlsruhe, Germany

[3] iBB Institute of Bioengineering and Biosciences, Instituto Superior Técnico, University of Lisbon, Avenida Rovisco Pais, Lisbon, Portugal

[4] Department of Industrial Engineering (DIN), Alma Mater Studiorum–University of Bologna, Bologna, Italy